Solution Structure of Component B from Methane Monooxygenase Derived through Heteronuclear NMR and Molecular Modeling[†,‡]

Shou-Lin Chang, Bradley J. Wallar, John D. Lipscomb, and Kevin H. Mayo*

Department of Biochemistry, Molecular Biology & Biophysics and Center for Metals in Biocatalysis, University of Minnesota, 435 Delaware Street, S.E., Minneapolis, Minnesota 55455

Received December 21, 1998; Revised Manuscript Received March 5, 1999

ABSTRACT: Methane monooxygenase (MMO) is a nonheme iron-containing enzyme which consists of three protein components: a hydroxylase (MMOH), an NADH-linked reductase (MMOR), and a small "B" component (MMOB) which plays a regulatory role. Here, ^{1}H, ^{13}C, ^{15}N heteronuclear 2D and 3D NMR spectroscopy has been used to derive the solution structure of the 138 amino acid MMOB protein in the monomer state. Pulse field gradient NMR self-diffusion measurements indicate predominant formation of dimers at 1 mM MMOB and monomers at or below 0.2 mM. MMOB is active as a monomer. Aggregate exchange broadening and limited solubility dictated that multidimensional heteronuclear NMR experiments had to be performed at a protein concentration of 0.2 mM. Using 1340 experimental constraints (1182 NOEs, 98 dihedrals, and 60 hydrogen bonding) within the well-folded part of the protein (residues 36−126), MMOB structural modeling produced a well-defined, compact α/β fold which consists of three α-helices and six antiparallel β-strands arranged in two domains: a $\beta\alpha\beta\beta$ and a $\beta\alpha\alpha\beta\beta$. Excluding the ill-defined N- and C-terminal segments (residues 1−35 and 127−138), RMS deviations are 1.1 Å for backbone atoms and 1.6 Å for all non-hydrogen atoms. Compared to the lower resolution NMR structure for the homologous protein P2 from the *Pseudomonas* sp. CF600 phenol hydroxylase system (RMSD = 2.48 Å for backbone atoms) (Qian, H., Edlund, U., Powlowski, J., Shingler, V., and Sethson, I. (1997) *Biochemistry, 36*, 495−504), that of MMOB reveals a considerably more compact protein. In particular, MMOB lacks the large "doughnut" shaped cavity reported for the P2 protein. This difference may result from the limited number of long-range NOEs that were available for use in the modeling of the P2 structure. This NMR-derived structure of MMOB, therefore, presents the first high-resolution structure of a small protein effector of a nonheme oxygenase system.

Multicomponent oxygenase systems often contain at least one component which serves an "effector" role (*1*−*10*). The exact nature of this role is different in each system, but it always involves the formation of a complex with the active-site-containing oxygenase component that alters the rate or specificity of catalysis in some way. One such effector protein is component B (MMOB)[1] from the soluble methane monooxygenase system isolated from methanotrophic bacteria (*9, 10*). Soluble and particulate methane monooxygenases (MMO) are the only enzymes that can catalyze the rapid oxidative cleavage of the extremely stable C−H bond of methane (*11*−*19*). The soluble form exhibits the following stoichiometry:

$$CH_4 + NADH + O_2 + H^+ \rightarrow CH_3OH + NAD^+ + H_2O$$

The presence of MMO in methanotrophic bacteria allows growth on methane as the sole source of carbon and energy (*14, 20*). As a result, these bacteria efficiently remove most of the biogenic methane from aqueous environments before it can be released into the atmosphere.

In addition to the 15 kDa MMOB, the soluble form of MMO from *Methylosinus trichosporium* OB3b consists of a 245 kDa hydroxylase component (MMOH) containing the active site and a 38 kDa reductase component containing FAD and a [Fe_2S_2] cluster (*10*−*13*). Although monooxygenase reactions that involve fissure of unactivated C−H bonds are often catalyzed by the heme enzyme, cytochrome P-450 (*21, 22*), this is not the case for methane (*14, 23, 24*). Rather MMOH contains a nonheme bis-μ-hydroxo bridged binuclear iron cluster in the active site that has been shown by kinetic and spectroscopic studies to be responsible for catalysis (*10, 24*−*30*). Most significantly, stopped flow and rapid quench

[†] This work was supported by National Institutes of Health (NIH) Grants R01-GM-40466 (J.D.L.) and Biophysics Training Grant GM-97323 (B.J.W.).

[‡] Coordinates have been deposited in the Brookhaven Protein Data Bank (2mob).

* To whom correspondence should be addressed at University of Minnesota, Department of Biochemistry, Molecular Biology, and Biophysics, 4-225 Millard Hall, 435 Delaware St. SE, Minneapolis, MN 55455. E-mail: mayox001@maroon.tc.umn.edu. Telephone: (612) 625-9968. Fax: (612) 624-5121.

[1] Abbreviations: NMR, nuclear magnetic resonance spectroscopy; rf, radio frequency; FID, free induction decay; CD, circular dichroism; MMO, methane monooxygenase; MMOH, MMO hydroxylase; MMOB, MMO component B; MMOR, MMO reductase; NOE, nuclear Overhauser effect; HSQC, heteronuclear single quantum correlation spectroscopy; HMQC, heteronuclear multiple quantum correlation spectroscopy; COSY, correlation spectroscopy; TOCSY, total correlation spectroscopy; PFG, pulsed field gradient, MOPS, 3-morpholinopropanesulfonic acid; DEAE, diethylaminoethyl; RMSD, root mean squared deviation; DSS, 4,4-dimethyl-4-silapentane; T4MOD, toluene monooxygenase component D; P2, phenol hydroxylase component P2.

10.1021/bi982992f CCC: $18.00
Published on Web 04/13/1999

```
                                  oo   o   o   o* o    * o    o   * ***   *
Pdx           1  -------------------MSKVVYVSHDGTRRELDVADGVSLMQAAVSNGIYDIVGDCG   27
MMOB          1  MSSAHNAYNAGIMQKTGKAFADEFFAEENQVVHESNAVVLVLMKSDEIDAIIEDIVLKGG   60
P2 (DmpM)     1  --------------------------------MSSLVYIAFQDNDNARYVVEAIIQD--   25
                                                 *  * o o   *o   oo* *o

                   o          o   ooo   o oo **o  *o        o*  * *       *
Pdx          28  GS------ASCATCHCYVNEAFTDKVPAANEREIGMLECVTAELKPN-SR-------LCC   87
MMOB         61  KAKNPSIVVEDKAGFWWIKADGAIEIDAAEAGELLGKPFSVYDLLINVSSTVGRAYTLGT  120
P2 (DmpM)    27  ---NPHAVVQHHPAMIRIEAEKRLEIRRETVEENLGRAWDVQEMLVDVITIGGNVDEDDD   82
                    **  **o o  o  *o*o  o**      * **o o * oo*oo* o  *

                   oo o* ** *o   o *
Pdx          88  QIIMTPELDGIVVDVPDRQW  107
MMOB        121  KFTITSELMGLDRALTDI    138
P2 (DmpM)    83  RFVLEWKN----------     90
                   o* o  o
```

FIGURE 1: Amino acid sequence comparisons between methane monooxygenase component B (MMOB) from *Methylosinus trichosporium* OB3b, the P2 component (DmpM) of phenol hydroxylase from *Pseudomonas* sp. CF600, and putidaredoxin (Pdx) from *Pseudomonas putida*. Sequences were aligned using the program ClustalW (*43*). Sequence comparisons are made to MMOB only. An asterik (*) indicates the presence of identical residues in the aligned sequences and an open circle (○) indicates homologous residues. Sequences were obtained for MMOB (*44*), P2 (*42*), and putidaredoxin (*45*).

kinetic techniques have been used to trap a unique bis-μ-oxo binuclear Fe(IV) intermediate termed compound Q (**Q**) during a single turnover of MMOH that was initially reduced to the diferrous state (*31, 32*) and then exposed to O_2. **Q** is the first monooxygenase intermediate capable of reacting directly with a range of hydrocarbons to yield hydroxylated, active-site-bound products.

Although MMOH in the absence of MMOB is capable of high yields of product formation from both single turnover and NADH/MMOR-coupled multiple turnover reactions (*10, 33*), the rates of these reactions are very slow, suggesting that MMOB has a very significant impact on catalysis. Accordingly, transient kinetic studies have revealed two major effects of MMOB on the turnover rate (*33*). First, it causes a 1000-fold increase in the rate of formation of a diferric peroxy intermediate (**P**) (*31, 34*) that results from the reaction of O_2 with diferrous MMOH. Second, it accelerates the formation of **Q** from **P** by about 40-fold, thereby maximizing its formation and preventing uncoupling due to nonproductive breakdown of **P**. These effects on catalysis are very dramatic such that essentially no **Q** accumulates in the absence of MMOB. The detailed mechanism by which MMOB regulates the conversion rates of the reaction cycle intermediates is unknown, but the effect is clearly mediated through the formation of a specific complex with the α-subunit of MMOH (*35*). Spectroscopic studies have shown that this complex alters the environment of the binuclear iron site (*35*−*38*). The conformational changes at the active site of MMOH induced by MMOB binding have other effects on catalysis as well. For example, it has been observed that the regiospecificity of hydroxylation for alternative MMO substrates that are more complex than methane is dramatically altered when MMOB is added (*39*), suggesting that their binding orientation in the active site is changed. Also, the redox potential of the binuclear iron site is changed dramatically when MMOB binds, causing a coupled change in the MMOH−MMOB affinity of approximately 5 orders of magnitude (*35, 38*).

The importance of complex formation and conformational changes in the role of effector proteins suggests that a fundamental understanding of their mode of action will require a knowledge of their three-dimensional structures. For the MMO system, structural studies have been limited to the MMOH component. The high-resolution X-ray crystal structures of MMOH from *M. trichosporium* OB3b (*25*) and *Methylococcus capsulatus* Bath (*26, 27*) have been reported. In contrast, neither MMOB nor its complex with MMOH has been successfully crystallized from either of the most commonly studied methanotroph species, and thus no structural data are currently available. High-resolution heteronuclear NMR spectroscopy offers an alternative approach to determining the three-dimensional structure of relatively small proteins such as MMOB. It has been used to determine the solution structures of two effector proteins, namely putidaredoxin from the cytochrome $P450_{cam}$ system (*40*) and protein P2 from the *Pseudomonas* sp. CF 600 phenol hydroxylase system (*6, 41, 42*). The latter component has significant sequence homology with MMOB as shown in Figure 1, and its associated oxygenase component contains a binuclear iron cluster like MMOH. This suggests that MMOB and P2 are relatively similar in both structure and function. However, MMOB is about 35% longer than P2 with a significant N-terminal extension that has no homology to the P2 sequence. The reported P2 structure is remarkable in that it reveals a large "doughnut" shaped cavity which has been proposed to have mechanistic significance, but the comparatively low resolution of the structure makes the presence of the cavity controversial (*6*). Solving the structure of MMOB may help clarify structural questions in this class of oxygenase effector proteins and would serve as the first step in determining the structural basis for the role of MMOB in catalytic regulation of the MMO system. Here, we report high-resolution NMR studies which have yielded the first structure of MMOB from an MMO system.

METHODS AND MATERIALS

Common reagents were the highest grade available and were obtained from either Sigma (St. Louis, MO) or Aldrich Chemicals (Milwaukee, WI). Molecular biological reagents were purchased from either Promega (Madison, WI), New England Biolabs (Beverly, MA), or Gibco BRL (Gaithersburg, MD). DEAE Sepharose and Sephadex G-50 resins were products of Pharmacia (Piscataway, NJ). ^2H_2O (99.9%) was purchased from either Cambridge Isotope Laboratory (Andover, MA) or Isotec, Inc. (Miamisburg, OH). ^{15}N-NH_4Cl (99%) and uniformly labeled ^{13}C-glucose (99%) were

obtained from Isotec, Inc. (Miamisburg, OH). Water was deionized and glass distilled or purified from deionized water using a Millipore reverse osmosis system. All sequence homology data were obtained through the use of either the Wisconsin Package (version 8.1) by Genetics Computer Group (Madison, WI) or by the program ClustalW (*43*).

Isolation of Recombinant MMOB. Starting with the entire methane monooxygenase gene cluster (*mmo*) from *M. trichosporium* OB3b (*44*, *46*) inserted into a pBluescript SKII vector (*47*), a section of DNA containing the MMOB gene (*mmob*) was excised based on the known gene sequence (*44*) and inserted into the pT7-7 vector (*48*). This construct gave a relatively low yield of protein in common expression systems. By cutting the plasmid with *Nde*I and *Stu*I to produce a cut at about 50 base pairs downstream from the *mmob* start codon, the excess DNA 5′ to the *mmob* gene was removed and was replaced with a short engineered duplex DNA oligonucleotide complementary to the *Nde*I and *Stu*I cut sites. The oligonucleotides were as follows: 5′-TATGTCCAGCGCTCATAACG CTTACAACGCCGGCAT-CATGCAGAA GACCGGCAAGG-3′ and 5′-CCTTGCCG-GTCTTCTGCATGATGCCGGCGTTGTAAGCGTTATG-AGCGCTGGACA-3′. This optimized the position of *mmob* with respect to the T7 promoter and ribosome binding site supplied by the pT7-7, and the resulting plasmid, pBWJ400, yielded high expression of *mmob* when subcloned into the BL21(DE3) strain of *Escherichia coli*. The *mmob* gene in pBWJ400 was sequenced by the Microchemical Facility (University of Minnesota) to confirm the accuracy of the new construct.

BL21(DE3) cells containing the pBWJ400 plasmid were cultured in M9-glucose medium (*49*) containing ampicillin (150 μg/mL) and grown at 37 °C either in 2 L flasks or 20 L glass fermentors with constant stirring and aeration. After reaching an o.d. = 0.8, cells were induced with 1 mM IPTG. After 2 h of further growth, cells were harvested and centrifuged at 9000*g* for 20 min at 4 °C. The cell paste was subsequently stored at −80 °C. Typically, 3 g of cell paste/liter of culture media was obtained. For the production of the isotopically labeled MMOB, the same growth procedure was used except the M9 medium contained ^{15}N-labeled NH_4-Cl and/or ^{13}C-glucose.

Purification of Recombinant MMOB. All steps of the purification procedure were carried out at 4 °C. The cell paste (30−75 g) was suspended in 100 mL of 25 mM MOPS, pH 7.0. Cells were sonicated for 2 min with a total of three repetitions while maintaining the temperature at 4 °C with a $CaCl_2$ ice bath, then diluted with an additional 350 mL of cold 25 mM MOPS, pH 7.0, and finally centrifuged at 25000*g* for 90 min. The supernatant was decanted and diluted with an additional 300 mL of 25 mM MOPS, pH 7.0. This cell-free extract was loaded immediately onto a fast-flow DEAE Sepharose column (40 mm × 330 mm) equilibrated with 25 mM MOPS, pH 7.0, at a linear flow rate of 20 cm/h. The column was then washed with 1L of 25 mM MOPS, pH 7.0, containing 0.08 M NaCl at a linear flow rate of 10 cm/h. The MMOB was eluted with a 1.6 L (800 mL × 800 mL) gradient from 0.08 to 0.25 M NaCl in the same buffer at a linear flow rate of 2 cm/h. Fractions were assayed for MMOB as previously described (*10*) and then pooled together. Solid $(NH_4)_2SO_4$ was added to the pooled MMOB fractions (50% of saturation) over 30 min, the mixture was centrifuged at 9000*g* for 30 min, and then the precipitant was resuspended in a minimal amount of 25 mM MOPS, pH 7.0. This was loaded onto a Sephadex G-50 column (44 mm × 1000 mm) equilibrated in the same buffer, and the material was eluted at 1 cm/h. The pooled fractions containing MMOB activity were concentrated via ultrafiltration, frozen in liquid nitrogen, and stored at −80 °C. Relative to native MMOB, recombinant MMOB exhibited the same molecular weight and electrophoretic properties, enhanced the rate of multiple turnover for a variety of substrates to the same extent, bound MMOH with the same high affinity, and promoted the formation of compound **Q** at the same rate.

Nuclear Magnetic Resonance (NMR) Spectroscopy. MMOB was dissolved in 0.6 mL of ^1H_2O or ^2H_2O containing 25 mM potassium phosphate, pH 6.8. The pH was adjusted by adding microliter increments of 0.1 M NaOH or 0.1 M HCl to the sample. In ^2H_2O, the pH was adjusted for the deuterium isotope effect. The solvent deuterium signal was used as a field-frequency lock. The chemical shifts are quoted in parts per million (ppm) downfield from sodium 4,4-dimethyl-4-silapentane sulfonate (DSS). All NMR experiments were run on Varian UNITY *plus* 600 and 800 MHz four-channel spectrometers equipped with a triple-resonance probe and a triple-axis gradient unit (University of Minnesota High Magnetic Field Facility) except the pulsed field gradient (PFG) diffusion measurements were carried out on the Bruker AMX 600 MHz spectrometer. NMR experiments for resonance assignments and structure determination were collected at 40 °C on 0.2 mM nonlabeled, ^{15}N single-labeled, and ^{13}C, ^{15}N double-labeled MMOB dissolved in 25 mM potassium phosphate buffer, pH 6.8. Depending on the sensitivity of the experiment, either 16 or 32 scans were acquired for each data point in the indirect dimension. Data were processed using Felix (Biosym), Varian VNMR, or NMRPIPE (*50*) and analyzed by NMRPIPP (*51*) on SGI workstations.

Pulsed Field Gradient NMR Self-Diffusion Measurements. To investigate MMOB self-association, NMR PFG diffusion measurements (*52*, *53*) were used essentially as described by Mayo et al. (*54*). In this technique, the constant magnetic field B_o is superimposed twice for a short time interval δ by additional inhomogeneous field gradient pulses $\Delta B_o = \pm Gz$. Between the two field gradient pulses, there is a time interval, Δ, in which $\delta \ll \Delta$. Under such conditions, when the spins diffuse, the dephasing effect of the first field gradient pulse on the magnetization cannot completely be refocused by the second field gradient pulse. A value for translational diffusion coefficient D can be obtained by fitting the data from a number of experiments performed using different values of G to change the extent of diffusion attenuation of the observed signal. The echo amplitude $A(t)$ is differentially attenuated in each spectrum due to translational diffusion. The physical process can be described by the expression

$$A(t) = A(0) \exp[-R(t) - (\gamma\delta G)^2(\Delta - \delta/3)D]$$

where $R(t)$ takes into account relaxation attenuation, γ = proton gyromagnetic ratio, δ = PFG duration (s), G = gradient strength (G/cm), Δ = time between PFG pulses (s), and D = translational diffusion coefficient. In order to obtain accurate D measurements, PFG strength was varied so that significant spin echo amplitude attenuation could be observed. The diffusion coefficient then can be calculated by fitting the above equation at different PFG strengths.

Table 1: Acquisition Parameters for NMR Experiments

experiment	carrier center (ppm) F1, F2, F3	no. of complex points F1, F2, F3	spectral width (Hz) F1, F2, F3	scans	field strength (MHz)	references
15N-edited NOESY-HSQC	4.73, 116.00, 4.73	64, 32, 512	9000, 2400, 9000	32	600	Zhang et al., 1994 (*56*)
13C-edited NOESY-HSQC	4.73, 35.00, 4.73	72, 62, 512	9500, 14 000, 9500	16	800	Muhandiram et al., 1993 (*57*)
15N-edited TOCSY-HSQC	4.73, 116.00, 4.73	64, 32, 512	9000, 2400, 9000	16	600	Zhang et al., 1994 (*56*)
H(CCO)NH	4.73, 116.00, 4.73	64, 32, 512	9000, 2400, 9000	16	600	Grszesiek et al., 1993 (*58*); Lyons et al., 1993 (*59*)
HNCA	56.00, 116.00, 4.73	64, 58, 512	4900, 2400, 9000	16	600	Yamazaki et al., 1994 (*60*)
HNCACB	46.00, 116.00, 4.73	64, 32, 512	12 000, 2400, 9000	16	600	Muhandiram et al., 1994 (*61*)
CACB(CO)NH	46.00, 116.00, 4.73	44, 58, 512	7500, 2400, 9000	16	600	Muhandiram et al., 1994 (*61*)
C(CO)NH	46.00, 116.00, 4.73	64, 32, 512	12 000, 2400, 9000	16	600	Grzesiek et al., 1993 (*58*); Lyons et al., 1993 (*59*)
HCCH-TOCSY	4.73, 35.00, 4.73	64, 48, 512	8000, 12 000, 8000	32	600	Kay et al., 1993 (*62*)
HNHA	4.73, 116.00, 4.73	64, 32, 512	9000, 2400, 9000	16	600	Kuboniwa et al., 1994 (*63*); Vuister et al., 1993 (*64*)
1H−15N HSQC	116.00, 4.73	256, 1024	2500, 12 000	32	800	Kay et al., 1992 (*65*)
NOESY	4.73, 4.73	256, 1024	9500, 9500	16	800	Wider et al., 1984 (*66*)
(HB)CB(CGCD)HD	35.0/125.0, 4.73	38, 1024	4800, 6000	256	600	Yamazaki et al., 1993 (*67*)
(HB)CB(CGCDCE)HE	35.0/125.0, 4.73	38, 1024	4800, 6000	256	600	Yamazaki et al., 1993 (*67*)
1H−13C CT-HSQC	125.0, 4.73	96, 2048	6300, 7000	32	800	Farmer et al., 1995 (*68*)

Diffusion data were acquired over a range of MMOB concentrations from 1.0 mM to 0.03 mM and at temperatures from 5 to 45 °C. Each diffusion constant was determined from a series of nine 1D PFG spectra acquired using different magnitudes of the magnetic field gradient pulses from 0, 5, 15, 25, 35, 45, 55, 65, to 75 G/cm. Experimental decay curves were approximated as single exponentials. Diffusion coefficients were calibrated and apparent molecular weights were estimated as described by Mayo et al. (*54*) by performing the same PFG NMR self-diffusion measurements on the globular proteins lysozyme, ribonuclease, and ubiquitin. The apparent molecular weight is related to the diffusion coefficient through the Stokes−Einstein equation as $D \propto M^{a}_{app}$, where the exponent a is equal to 1/3 for compact molecules (*55*). The apparent molecular weight of component B is calculated by comparing its diffusion constant with those of the standard proteins listed above.

Heteronuclear NMR Experiments. Sequence specific resonance assignments, determination of $^{3}J_{HN\alpha}$ coupling constants, and derivation of NOE distance constraints were made through analysis of experiments listed in Table 1 (*56*−*68*). On the 600 MHz NMR spectrometer, a total of 64(t1) × 32(t2) × 512(t3) complex data points were collected for 3D ^{15}N-edited TOCSY-HSQC (mixing time 60 ms), ^{15}N-edited NOESY-HSQC (mixing time 75, 100, 150, and 200 ms), H(CCO)NH, and HNHA experiments with spectral widths of 9000, 2400, and 9000 Hz in each dimension, respectively. The carrier frequency for ^{1}H and ^{15}N was positioned at 4.73 and 116.0 ppm, respectively. 3D HNCA, HNCACB, CACB(CO)NH, and C(CO)NH experiments were acquired on a 600 MHz spectrometer. A total of 64(t1) × 32(t2) × 512(t3) complex data points were collected with spectral widths of 4900, 12 000, 7500, and 12 000 Hz in the t1 ^{13}C dimension, respectively. The spectral width for the t2 ^{15}N dimension was 2400 Hz, and for the 13 proton dimension, it was 9000 Hz. The t1 carrier frequency in the HNCA experiment was positioned at 56 ppm, whereas it was positioned at 46 ppm for all other NMR experiments. The ^{1}H and ^{15}N carrier frequencies were positioned at 4.73 and 116.0 ppm, respectively.

The 3D HCCH-TOCSY experiment (mixing time, 15.6 ms) was acquired on a 600 MHz NMR spectrometer. A total of 64(t1) × 48(t1) × 512(t3) complex data points were collected with spectral widths of 8000, 12 000, and 8000 Hz in each dimension, respectively. The ^{13}C channel was positioned at 35 ppm, and the ^{1}H carrier frequency was positioned at 4.73 ppm. ^{13}C-edited NOESY experiments (mixing times of 100 and 150 ms) were acquired on the 800 MHz NMR spectrometer. A total of 72(t1) × 62(t2) × 512(t3) complex data points were collected over spectral widths of 9500, 14 000, and 9500 Hz in each dimension, respectively. The ^{1}H carrier frequency was positioned at 4.73 ppm, and the ^{13}C carrier frequency was positioned at 35 ppm. Prior to Fourier transformation, each 3D data set was apodized using a shifted squared sine-bell window function to enhance resolution and was zero filled to 128 × 128 × 1024 complex data points.

Interproton distance restraints were derived from NOEs assigned in 3D ^{15}N-edited NOESY (mixing times 75, 100, 150, 200 ms) and 3D ^{13}C-edited NOESY (mixing times 100 and 150 ms) spectra. Analysis of NOE growth curves indicated that while backbone to backbone interproton NOEs were normally maximum at 100 ms, side chain to side chain and some side chain to backbone NOEs were maximum at 100−200 ms. Generally 100 and 150 ms data sets were used to get the approximate interproton distance. NOE restraints were grouped into four distance ranges: 1.8-2.7 Å (1.8−2.9 Å for NOEs involving NH protons), 1.8−3.3 Å (1.8−3.5 Å for NOEs involving NH protons), 1.8−5.0 Å, and 1.8−6.0 Å, corresponding to strong, medium, weak, and very weak NOEs, respectively (*69*). Pseudo-atom corrections were added to the upper bound distance constraints where appropriate (*70*), and a 0.5 Å correction was added to the upper bound for NOEs involving methyl protons (*71*, *72*). Averaging was applied to NOEs involving nonstereospecifically assigned methylene protons (*73*, *74*). In addition, torsion angle restraints were derived using $^{3}J_{HN\alpha}$ coupling constants obtained from a 3D HNHA experiment. Dihedral angle restraints for these ϕ angles were set to ($-120° \pm 30°$) when $^{3}J_{HN\alpha}$ was greater than 9 Hz, ($120° \pm 50°$) when $^{3}J_{HN\alpha}$ was between 8 and 9 Hz, and ($-60° \pm 30°$) when $^{3}J_{HN\alpha}$ was less

than 6 Hz (*75*). Hydrogen bond constraints were identified from the pattern of sequential and interstrand NOEs involving NH and CαH protons, chemical shift index, and together with evidence of slow amide proton−solvent exchange experiment. Exchange of amide protons was monitored with a series of 2D $^{1}H-^{15}N$ HSQC experiments performed at 40 °C. An aliquot of 2 mM MMOB dissolved in $^{1}H_2O$ was mixed into a $^{2}H_2O$ solution to achieve a final concentration of 0.2 mM and to allow amide protons to exchange for deuterons. Each HSQC spectrum took 30 min to collect. For each hydrogen bond identified, two distance constraints were used: 1.6−2.4 Å for H−O constraints and 2.6−3.4 Å for N−O constraints.

Computer Modeling. NMR/NOE-derived internuclear distance constraints were used in calculating structures for MMOB. Structure calculations were performed using the program XPLOR 3.851 (*76*) on a SGI Origin 2000 with 32 R10K 195 MHz CPUs and 8 Gbyte RAM running IRIX 6.5.1 at Minnesota Supercomputer Institute. MMOB was created using parallhdg.pro force fields. For NOE constraints, a soft potential function was used. NMR structures were generated using the ab initio simulated annealing (SA) protocol starting from a template coordinate set (*77*). First a starting template was generated by placing the macromolecule along the *x*-axis, with *y* and *z* set to random numbers. The template coordinates were then regularized using simulated annealing to get good local geometry and remove nonbonded contacts. The SA protocol started with 50 cycles of Powell minimization (*78*) followed by 80 ps Verlet dynamics at high temperature (3000 K). During this period, the NOE pseudo-potential was applied with soft asymptotic behavior, switching between harmonic and asymptotic regions at a constant value of 0.5 Å. The weight on the quartic van der Waal (vdW) term was set to a very low value (0.002 kcal mol^{-1} Å^{-4}) to allow atoms to pass through each other. At the next stage, 40 ps Verlet dynamics at 3000 K was performed. The asymptote of the NOE potential was tilted from 0.1 to 1 at this stage to increase weights on geometry. The final stage of the SA protocol was to cool the system down to 100 K (*79*). During the cooling stage, the temperature dropped at the 50 K step. The vdW radius was set at 0.9 Å initially and then reduced step by step to 0.75 Å. The vdW force constant started from 0.003 kcal mol^{-1} Å^{-4} and increased to a final value of 4.0 kcal mol^{-1} Å^{-4}. The structures generated were subjected to another 1000 steps of Powell minimization. At the *ab initio* annealing stage, only the NOE restraints were included in the calculation. The dihedral restraints and hydrogen bond restraints were introduced at the final stage of structure refinement based on simulated annealing starting at 1000 K and ending at 100 K. Final structures were selected under the criteria that no NOE violations greater than 0.5 Å; no dihedral angle violations greater than 5°; no angle, bond length, and improper deviated from ideal geometry greater than 5°, 0.05 Å, and 5°, respectively, were allowed.

Structures were then analyzed, displayed, and superimposed by using either the BIOSYM INSIGHT viewer (Biosym) or MolMol (*80*) and XPLOR subroutines.

RESULTS

Assessing the State of Aggregation. MMOB is known to self-associate in solution (*35*). ^{1}H NMR spectra of 1 mM MMOB display broader resonances than expected for a globular protein of molecular weight 15 000 Da. As the concentration is lowered, line widths decrease, indicating dissociation of MMOB aggregates. Below about 0.2 mM, line widths do not appear to change and are consistent with those expected for monomeric MMOB as shown in Figure 2. Resonance dispersion in this ^{1}H NMR spectrum of MMOB indicates that the protein is folded compactly.

To better address MMOB aggregation, pulsed field gradient (PFG) NMR self-association diffusion measurements were performed. Translational diffusion coefficients, *D*, derived from these data (*54*) are plotted as a function of MMOB concentration at 15 °C in Figure 2 (lower inset). At the lowest three concentrations measured, *D* values are nearly the same, indicating that MMOB dissociation is mostly complete. As the concentration is increased, *D* decreases as expected with increasing aggregation. The Stokes−Einstein equation $D = k_B T/6\pi\eta R$ was used to relate *D* to the macromolecular radius, *R*, which for globular proteins is proportional to $M^{1/3}_{app}$ where M_{app} is the apparent molecular weight (*55*). Relative to M_{app} and measured *D* values for standard proteins lysozyme, ribonuclease, and ubiquitin, *D* values for MMOB indicate that at 15 °C it has an average molecular weight of a dimer at concentrations of about 1 mM and monomer at 0.13 mM and below. For protein standards, apparent molecular weights calculated from PFG NMR-derived diffusion constants are in good agreement with their actual molecular weights, and even though the actual molecular shape and the shape of the molecular aggregate would be expected to affect the diffusion coefficient, the maximum change, for example, in D_{dimer} due to geometry compared to *D* of a spherical molecule of equal volume would only be about 5% (*81*). From these PFG NMR diffusion data, an apparent equilibrium dissociation constant, K_D, was estimated to be about 0.5 mM at 15 °C.

The presence of primarily monomeric MMOB at 0.13 mM was confirmed by measuring *D* as a function of temperature (Figure 2, upper inset). Between 15 and 45 °C, the curve is linear following an Arrhenius relation with the same activation energy as for the self-diffusion of water, i.e., 4.8 kcal/mol (*82*), and paralleling that found for monomeric lysozyme at a similar concentration (Figure 2). These data indicate that MMOB remains monomeric over this temperature range. At 15 °C, *D* deviates somewhat from this slope, suggesting that at this lower temperature some MMOB aggregation is occurring. This is supported by the observation that at 1 mM MMOB decreasing the temperature significantly increases aggregation. In this respect, PFG self-diffusion data indicate that working in water at relatively low MMOB concentrations (0.2 mM and below), low salt, and temperatures greater than 25 °C defines good solution conditions for maintaining MMOB primarily in the monomeric state. Conditions which maintain MMOB primarily in the monomer state and allow for good spectral signal-to-noise were found with 0.2 mM MMOB dissolved in 25 mM potassium phosphate, pH 6.8, at a temperature of 40 °C.

^{1}H, ^{15}N, ^{13}C Resonance Assignments. Figure 3 shows the 2D ^{15}N HSQC spectrum of MMOB at 40 °C. A total of 136 cross-peaks are detected: 122 peaks (three of them are not shown in the spectrum because they are under the plot level) from backbone amide, 2 from the indole NHs of tryptophans, and 13 from the side chain NHs of arginine, glutamine, and

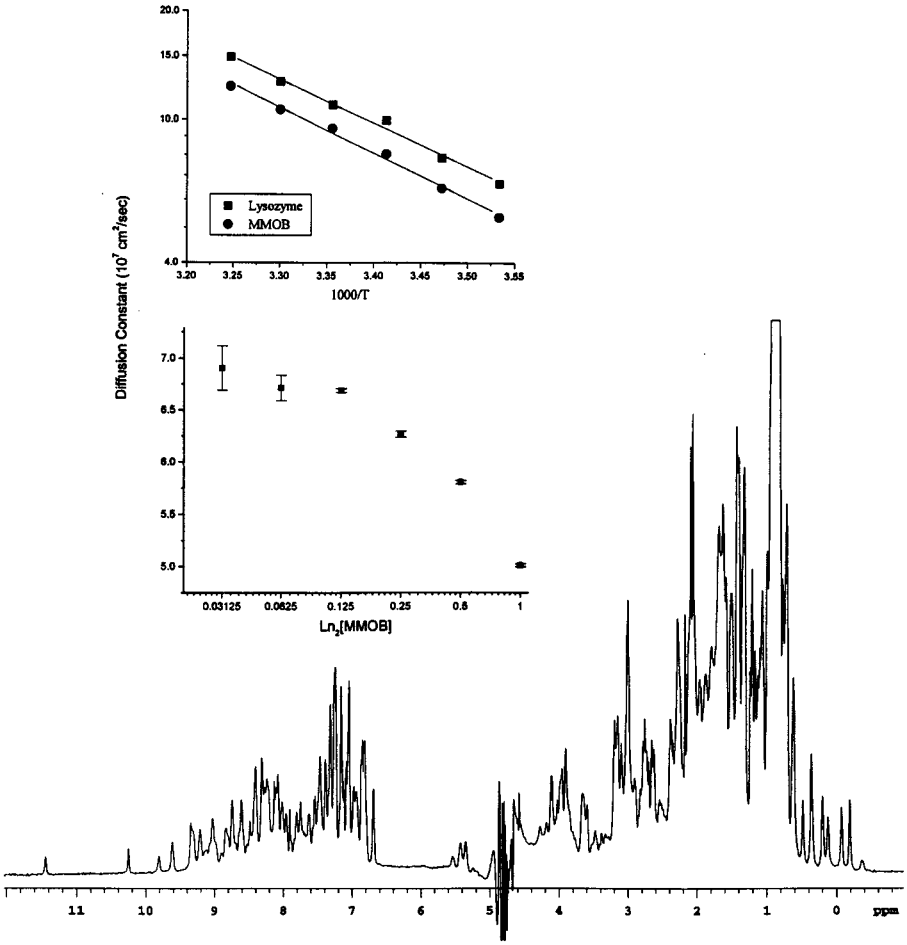

FIGURE 2: ^{1}H NMR spectrum and diffusion measurements of MMOB. A 600 MHz ^{1}H NMR spectra of MMOB is shown at the bottom of the figure. It was accumulated at 0.2 mM MMOB in ^1H_2O. The solution contained 25 mM potassium phosphate, pH 6.8, 40 °C. Correction was made for the deuterium isotope effect. Pulsed-field gradient (PFG) NMR-derived translational diffusion coefficients are shown in the two panel insets to the figure. The lower panel inset has diffusion coefficients plotted as a function of MMOB concentration (15 °C), and the upper panel insert has diffusion coefficients plotted at 0.13 mM MMOB as a function of the inverse temperature (K^{-1}). Data for one of the standard proteins, lysozyme, which was used to calibrate diffusion coefficient measurements and to derive apparent molecular weights for MMOB, are shown in the upper panel. Experimental conditions were as follows: $\delta = 4$ ms, $g = 1$ to 45 G/cm, $\Delta = 34.2$ ms, and the longitudinal eddy-current delay $T_e = 100$ ms. MMOB was dissolved in ^2H_2O under the same solution conditions described above.

asparagine. Since there are two prolines in the sequence and normally the N-terminus residue cannot be observed, the theoretical number of backbone amide resonances should be 135. Of the 122 detected backbone amide resonances, 121 were assigned. Almost all of the 14 missing signals can be attributed to N-terminal residues (M1 to E23) with exceptions Q30 and G119. This may be due to flexibility and slow conformational exchange of the N-terminal region in solution. The unidentified cross-peak is marked with an "x" in the spectrum.

For the assignment process, spin systems were identified initially by analyzing cross-peaks in 3D HCCH-TOCSY, ^{15}N-edited TOCSY-HSQC, HNCA, HNCACB, CBCACONH, C(CO)NH, and H(CCO)NH. Spin systems were then categorized into two groups: the first contains spin systems correlated with their attached amide group NH(i); the second contains those correlated with the following amide group NH($i + 1$). Sequential connectivities were established by matching spin systems from those two types. Sequence-specific resonance assignments were made by starting from spin systems which have distinct characteristics such as glycine, serine, and threonine, for they have easily recognized C_α and C_β, respectively. Using these as starting points, sequence-specific assignments were extended to both sides of the sequence. This is exemplified in Figure 4 which shows several ^{15}N planes from HNCACB and CACBCONH experiments. Arrows indicate how through-bond connectivities and resonance assignments were made.

Aliphatic side chain ^{1}H and ^{13}C resonances were assigned by analyzing the 3D ^{15}N-edited TOCSY-HSQC, 3D H(CCO)NH, and 3D C(CO)NH spectra. Assignments were confirmed by analyzing results from a 3D HCCH-TOCSY experiment. Aromatic side chain resonances from tyrosine, phenylalanine, and tryptophan were assigned by analyzing 2D proton homonuclear TOCSY in D_2O, 2D (HB)CB(CGCD)HD, and 2D (HB)CB(CGCDCE) HE spectra. The ϵ-proton and -carbon of histidine were assigned by using a 2D ^{13}C CT-HSQC experiment. Assignments were confirmed by detection of NOEs from the aromatic side chain to intraresidue Hβs and Hαs. Tryptophan indole ^{1}HN and ^{15}N resonances were assigned by detection of NOEs to its intra side chain protons in 3D ^{15}N-edited NOESY-HSQC spectra. All known ^{1}H, ^{15}N, and ^{13}C resonance assignments are provided in Table 2 of the Supporting Information.

Secondary Structure and Overall Folding. The secondary structure of MMOB was derived using standard NMR

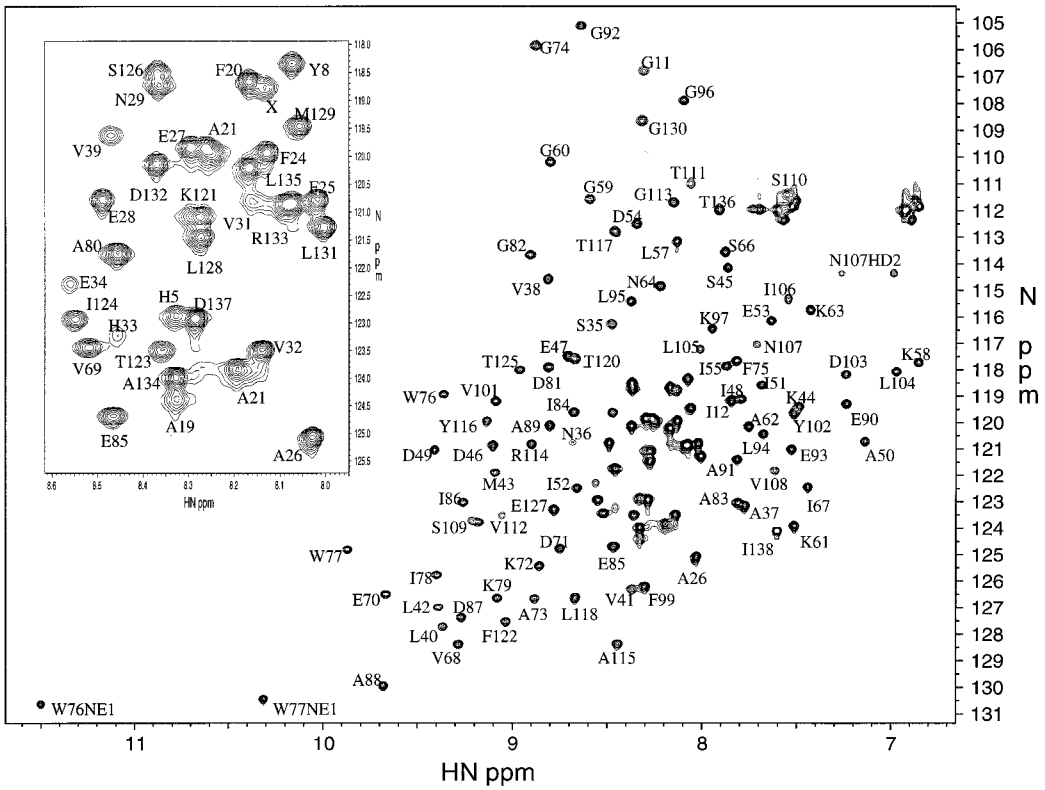

FIGURE 3: ^{15}N HSQC spectrum of MMOB. A 2D ^{15}N HSQC NMR spectrum of MMOB is shown. Protein concentration was 0.2 mM in 25 mM potassium phosphate at pH 6.8 and 40 °C. Cross-peaks have been labeled based on assignments made via analysis of through-bond connectivities. The panel inset at the upper left of the figure is an expansion of the more crowded mid-region of the spectrum. Solution conditions are given in the legend to Figure 2.

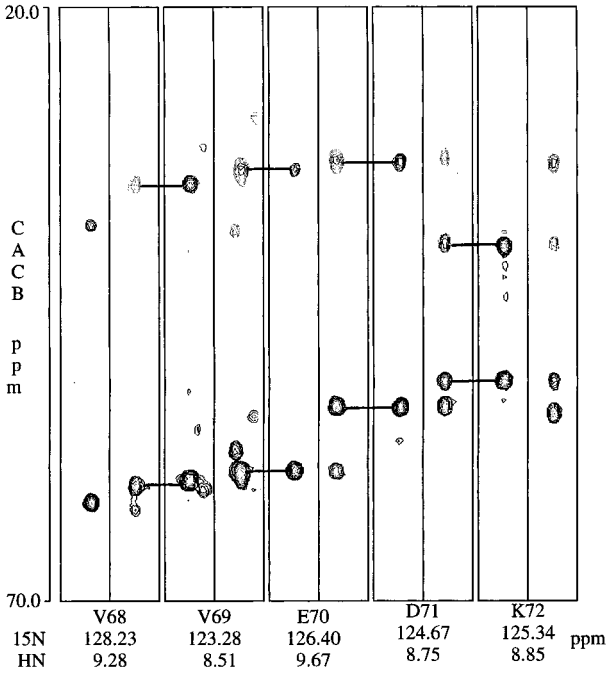

FIGURE 4: Through-bond sequential assignments in MMOB. To exemplify how through-bond sequential assignments were made, several ^{15}N planes from HNCACB and CACBCONH experiments have been plotted as indicated. Horizontal lines between ^{15}N planes indicate how through-bond connectivities and resonance assignments were made. Solution conditions are given in the legend to Figure 2.

criteria, i.e., analysis of backbone NOEs, $^{3}J_{NH\alpha}$ coupling constants, the chemical shift index, and hydrogen−deuteron exchange experiments. These results along with elements of regular secondary structure are summarized in Figure 5. The secondary structure of MMOB consists of an aperiodic N-terminus (residues 1−36) which leads into the first β-strand (residues 37 to 43) followed by a segment of α-helix (residues 47−62). After a short loop, a series of three, tight-turn connected, β-strands (residues 67−72, 75−80, and 83−87) lead into an α-helix loop α-helix (residues 89 to 107) motif. A rather extended loop (residues 108 to 114) follows and culminates at the C-terminus in two β-strands (residues 115−118 and 121−125) and a final aperiodic segment (residues 126−138).

Even at this stage of the structural analysis, the overall folding into antiparallel β-sheet is evident in NOESY data as exemplified in Figures 6 and 7. Figure 6 shows three ^{13}C planes from a ^{13}C-edited NOESY data set. The panel on the left shows cross-strand NOEs between D87 (β-strand 4) and K121 (β-strand 6) and between N36 (β-strand 1) and S126 (β-strand 6). The N36/S126 pairing is also evident in the middle panel along with side chain to side chain NOEs between V41 (β-strand 1) and S109 (a loop). The 2D homonuclear NOESY plot of the αH−αH region in Figure 7 shows most of these cross-strand αH−αH NOEs which were initially fully identified in 3D heteronuclear NOESY experiments. This type of NOE information was used to identify regions of antiparallel β-sheet structure in MMOB as depicted at the right in Figure 7.

Molecular Modeling of the MMOB Structure. Interproton distance restraints were derived from NOESY type experiments such as 2D proton homonuclear NOESY (mixing time 150 ms), 3D ^{15}N-edited NOESY-HSQC (mixing times 75, 100, 150, 200 ms), and 3D ^{13}C-edited NOESY-HSQC

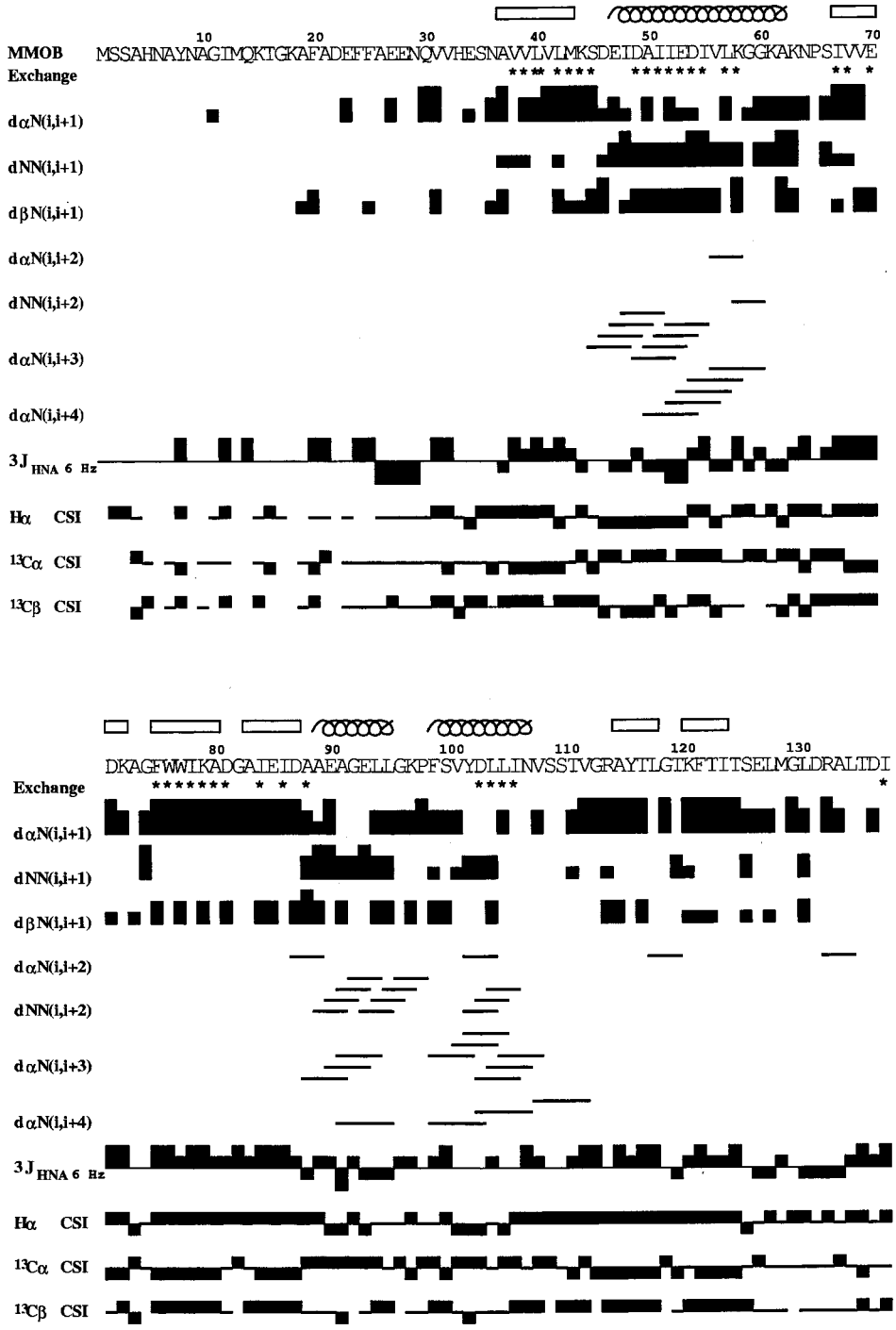

FIGURE 5: Secondary structure elements for MMOB. The secondary structure of MMOB was derived by analysis of backbone NOEs, $^3J_{NH\alpha}$ coupling constants, the chemical shift index, and hydrogen−deuteron exchange experiments. These results along with elements of regular secondary structure are summarized in this figure.

(mixing time 150 ms). A total of 1182 distance restraints from the well-structured part of MMOB (residues 36−126) were derived from cross-peak intensities from 3D ^{15}N-edited NOESY-HSQC and 3D ^{13}C-edited NOESY-HSQC spectra. These NOE restraints include 575 intraresidue restraints, 332 sequential restraints, 140 medium-range restraints ($|i - j| \leq 4$), and 135 long-range NOEs ($|i - j| > 4$). Approximate interproton distance restraints were grouped into four distance ranges: 1.8−2.7 Å (1.8−2.9 Å for NOEs involving NH protons), 1.8−3.3 Å (1.8−3.5 Å for NOEs involving NH protons), 1.8−5.0 Å, and 1.8−6.0 Å, corresponding to strong, medium, weak, and very weak NOEs, respectively. Distances involving methyl groups and aromatic ring protons were represented as $(\sum r^{-6})^6$ sum. In addition, 98 ϕ torsion angle restraints were derived using $^3J_{HN\alpha}$ coupling constants obtained from a 3D HNHA experiment as described in the Methods Section. Hydrogen bond restraints (two for each of the 30 hydrogen bonds) identified by the presence of long-lived hydrogen bonds from hydrogen−deuteron exchange experiments and from NOE patterns were introduced during the final stage of structure refinement.

The 3D structure calculation of MMOB was based, therefore, on 1340 experimental restraints from the well-structured part of the protein (residues 36−126). This

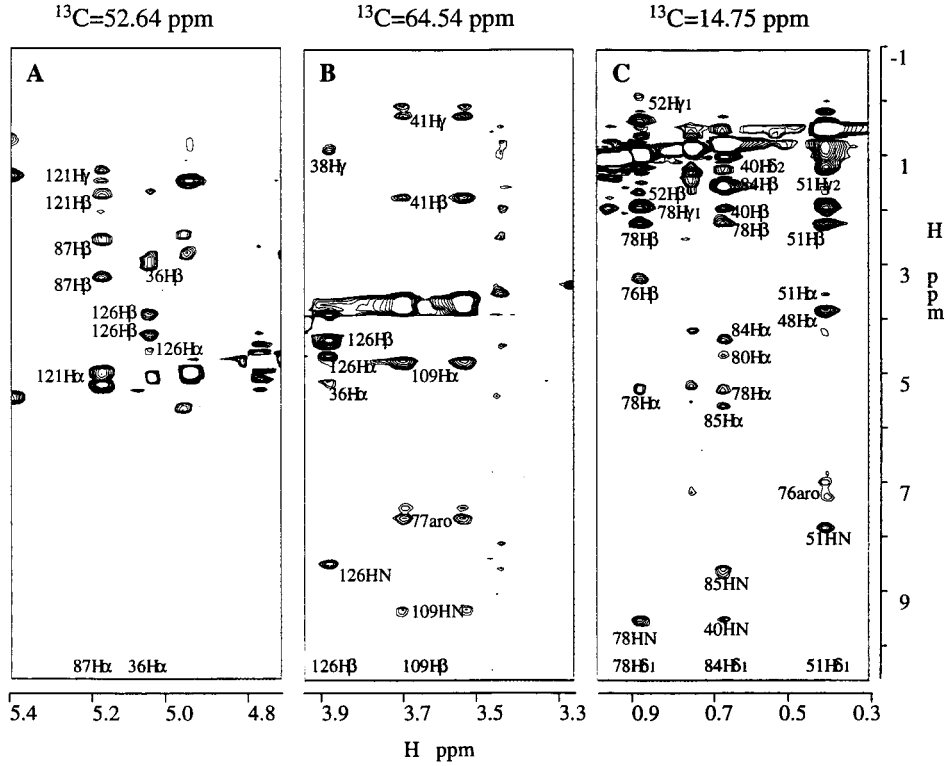

FIGURE 6: ^{13}C-edited NOESY data of MMOB. Three ^{13}C planes from a 3D NMR ^{13}C-edited NOESY data set are shown. Carbon frequencies in ppm are given above each panel in the figure. These NOESY data were acquired either in $^{2}H_2O$ (panel A) or in $^{1}H_2O$ (panels B and C). Solution conditions are the same as those given in the legend to Figure 2.

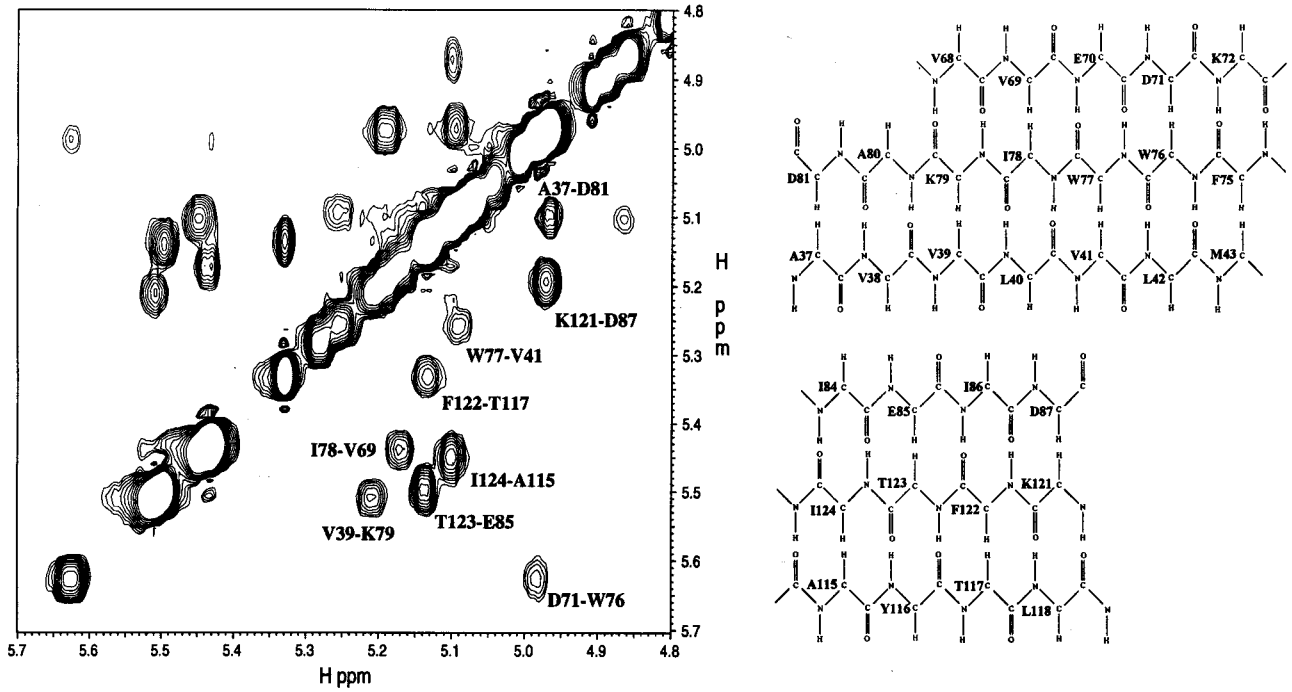

FIGURE 7: ^{1}H NOESY and β-strand alignments in MMOB. The spectrum at the left shows the αH−αH region from a ^{1}H NOESY data set acquired in $^{2}H_2O$ with solution conditions being the same as those given in the legend to Figure 2. Labeled cross-peaks identify cross-strand αH−αH pairings in the antiparallel β-sheet regions in MMOB. These β-sheets in MMOB are depicted schematically at the right in the figure.

translates into about 13 restraints per residue. A superposition of the 15 best structures from 50 starting structures is shown from two perspectives in Figure 8, and ϕ,ψ backbone angles for the average structure are provided in the Ramachandran plot in Figure 9. MMOB is rather oblate in shape. The view at the left of the figure shows MMOB looking down the short axis, whereas the view at the right looks down one of the long axes. For these 15 structures, there were no NOE violations greater than 0.5 Å and no dihedral angle violations greater than 5°. A summary of structural statistics is provided in Table 2. Within the well-structured part of the protein (residues 36−126), the Cartesian RMS deviation from an

Table 2: Structural Statistics

RMS deviations from experimental distance restraints	
NOE (1182) plus H-bond (60) (Å)	0.074 ± 0.002
RMS deviations from experimental dihedral restraints (deg)	0.6 ± 0.1
deviation from idealized geometry	
bonds (Å)	0.005 ± 0.0002
angles (deg)	0.70 ± 0.03
impropers (deg)	0.53 ± 0.02
energies (kcal mol^{-1})	
E_{NOE}	363 ± 19
E_{CDH}	2.4 ± 0.7
E_{bond}	56 ± 5
E_{angle}	284 ± 23
$E_{improper}$	46 ± 3
E_{total}	867 ± 56

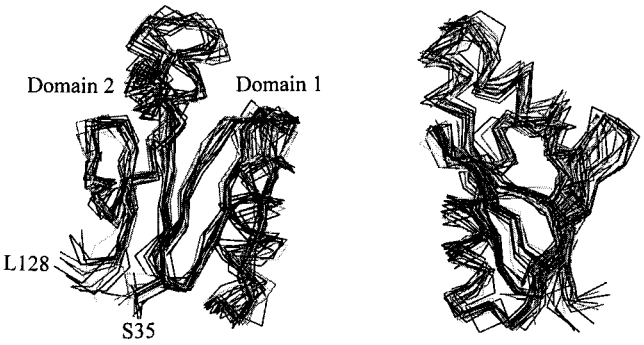

FIGURE 8: Calculated structures for MMOB. 3D structure calculation of MMOB was based on 1340 NMR-derived experimental restraints from the well-structured part of the protein (residues 35−128). A superposition of the 15 best structures is shown in this figure. Only the Cα trace is shown. Structures on the left have been rotated 90° relative to those on the right of the figure.

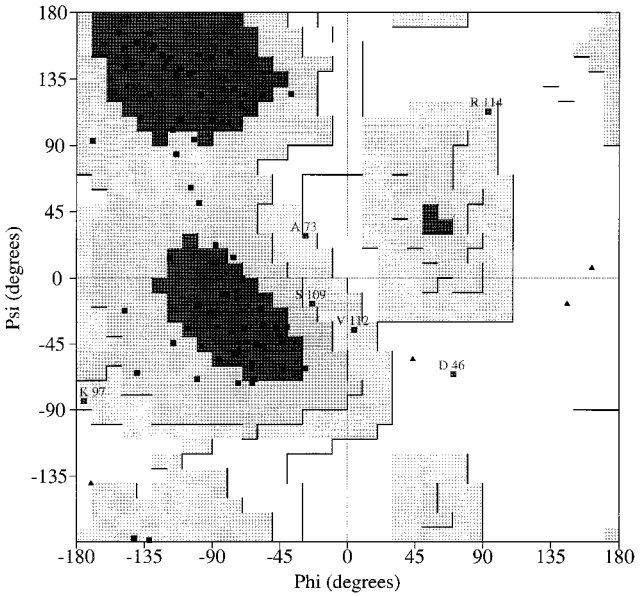

FIGURE 9: Ramachandran plot for MMOB. This Ramachandran plot shows the ϕ,ψ angle distribution for the average structure of MMOB. Only residues within the well-structured region (residues 35−128) of MMOB have been plotted. By analyzing this plot using PROCHECK (*83*), the percentage of residues in most favored regions is 63.4%, in additional allowed regions is 31.9%, in generously allowed regions is 3.0%, and in disallowed regions is 1.7%. Residues which fall into the disallowed region are D46, A73, and V112.

average structure is 1.1 Å for backbone atoms and 1.6 Å for all non-hydrogen atoms.

MMOB consists of two domains. The first domain starts from residue N36−D81, and the second domain is from G82−S126. Domain one (labeled as number "1" in Figure 8) consists of three β-strands (strand 1: A37-M43, strand 2: I67-K72, and strand 3: F75-A80) and an α-helix (helix 1: E47-A62). Strand 3 is antiparallel paired with strand 1 and strand 2 with helix 1 sitting on top of this β-sheet scaffold. Domain two (labeled as number "2" in Figure 8) also consists of three β-strands (strand 4: A83-D87, strand 5: A115-L118, and strand 6: K121-T125) and two α-helices (helix 2: A89-L95 and helix 3: F99-N107). Strand 6 is antiparallel paired with strands 4 and 5. The contact interface between the two domains is primarily located at strand 1 and V108-S110. The N-terminus (M1-S35) and C-terminus (E127-I138) show no long-range NOEs with domains one or two.

Insight into the possible preferred conformation of N-terminal and C-terminal residues comes from a circular dichroic (CD) spectrum of MMOB (data not shown) which is typical for an α/β protein (*84*). α-Helix conformation gives a negative CD band at 222 nm, while β-sheet conformation gives a negative CD band at 216 nm, and turn and random coil (or aperiodic) structure yields negative CD bands more toward the far-UV. Upon deconvolution of the CD trace using the program of Provencher (*85*), MMOB was found to be comprised of 32% α-helix, 20% β-sheet, 27% turn, and 21% other. This estimate of β-sheet is essentially the same as that deduced from the NMR-derived structure of the well-folded part of MMOB. Helix and turn contents deduced from the NMR structure, however, are only 24% and 20%, respectively. The 8% difference in helix and the 7% difference in turn content indicates that the N- and C-termini probably have transient helical/turn structure which may be "locked in" on binding to MMOH.

Substrate Effects on the MMOB Structure. In the presence of excess methane or furan (substrates for the MMO system), no significant chemical shift changes were observed in MMOB at 0.2 mM. Therefore, these substrates do not appear to bind to or associate with MMOB, which argues against a role for MMOB−substrate interaction in the catalysis by MMO.

DISCUSSION

In this study, the three-dimensional solution structure of MMOB, the effector protein from the MMO enzyme system, has been determined. Effector proteins from oxygenase systems generally fall into two categories. Some, such as

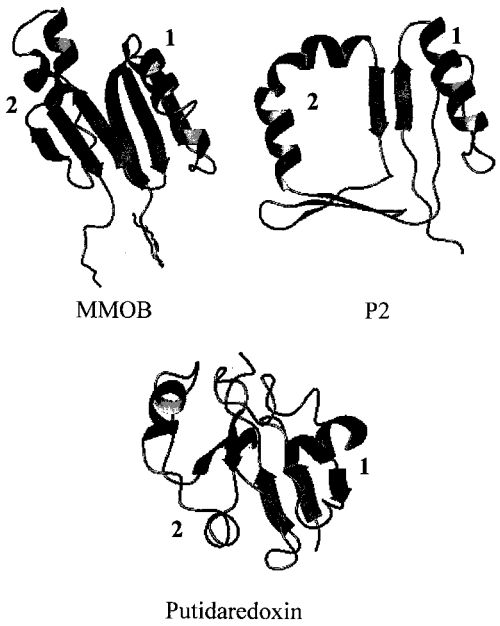

FIGURE 10: Structural comparison of MMOB, P2, and putidaredoxin. Backbone folds of NMR-derived structures of MMOB, P2 (*6*), and putidaredoxin (*40*) are depicted as ribbon drawings. Atomic coordinates were taken from the Brookhaven Protein Structural Data Base using pdb access codes 1hqi for P2 protein and 1put for putidaredoxin. Domains one and two are labeled as "1" and "2", respectively, in the figure.

the $[Fe_2S_2]$ cluster-containing putidaredoxin from the $P450_{cam}$ monooxygenase system, also serve to transfer electrons to the oxygenase component (*1, 2*). Others are devoid of redox cofactors and must transmit their effects solely through complex formation and conformational change. MMOB is the archetypal protein in the latter class, but many others recently have been identified based, in part, on screening of genomes for sequence homologies to the binuclear iron cluster binding region of MMOH (*86*). These include the small protein components of the toluene 2-monooxygenase from *Burkholderia cepacia* G4 (*3*), the toluene 4-monooxygenase (T4MOD) from *Pseudomonas mendocina* KR1 (*4, 5*), the phenol hydroxylase (P2) from *Pseudomonas* sp. CF600 (*6*), and the alkene monooxygenase from *Xanthobacter* strain Py2 (*7*) and *Nocardia corallina* b-276 (*8*) systems. Comparison of the NMR solution structures of MMOB, P2 (*6*), and putidaredoxin (*40*) shows that they are all α/β proteins consistent with the presence of some degree of sequence homology (see Figure 1). Nevertheless, their structures have significant differences which are discussed here. Figure 10 shows all three structures as backbone ribbon diagrams with domain one (labeled with the number "1") of MMOB oriented to the right in the figure.

Although both MMOB and putidaredoxin appear to accelerate formation of a reactive high-valent iron species in the catalytic cycle that is responsible for substrate hydroxylation (*1, 2, 33, 87*), they function, in many respects, quite differently as effector molecules. Putidaredoxin forms a complex with $P450_{cam}$ at two stages in the catalytic cycle (*1, 2*). Its first function is a relatively nonspecific single-electron transfer to reduce $P450_{cam}$ in preparation for reaction with O_2. Putidaredoxin then forms a second, highly specific complex with oxy-$P450_{cam}$ to transfer the second electron required for catalysis (*1, 2, 87*). While many general electron transfer reagents can perform the first transfer to $P450_{cam}$, only putidaredoxin can transfer the second electron efficiently, suggesting that conformational changes induced by complexation play a role in the overall reaction process. In contrast to this function of putidaredoxin, MMOB from *M. trichosporium* OB3b does not appear to have any significant affect on the electron transfer process in the MMO system.[2] Rather, its major role is in accelerating the reaction with O_2, a reaction which is apparently unaffected by the presence of putidaredoxin in the $P450_{cam}$ system (*1*).

Despite the fact that putidaredoxin has a 40% sequence similarity with MMOB and possesses similar secondary conformational features, the overall folds of these two proteins are quite different. Like MMOB, putidaredoxin (Figure 10) is composed of two folding domains: one $\beta\beta\alpha$ (oriented as with MMOB, to the right in Figure 10) and one $\beta\alpha\alpha\beta\beta\beta$. Its amino acid sequence between helix 3 and β-strand 6 is more like a long loop containing short β-strands 4 and 5. The first domain from the N-terminus has a $\beta\beta\alpha$ motif where the α-helix orthogonally crosses a two-stranded antiparallel β-sheet. In MMOB, the first domain is folded in a $\beta\alpha\beta\beta$ motif where the α-helix runs almost parallel to the antiparallel β-sheet comprising these first three β-strands. In putidaredoxin, a third strand (C-terminal β-strand 6) from domain two runs parallel to β-strand 1 in domain one. This structural motif of the first domain from putidaredoxin is also nearly the same as that from *Anabaena* ferredoxin (*88*) which contains a similar Fe_2S_2 cluster.

Similarities between the structures of MMOB and putidaredoxin also can be observed in domain two where in both proteins a β-strand (4 and 3, respectively) leads into a helix−loop−helix motif with both helices 2 and 3 from both proteins being short two-turn helices. In MMOB, these helices are folded compactly together, whereas in putidaredoxin, they are separated by an intervening long loop containing β-strands 4 and 5 mentioned above. Although MMOB and putidaredoxin structural folds are different, their conformational similarities are consistent with an evolutionary link. The absence of the iron sulfur moiety in MMOB may help to explain folding differences relative to putidaredoxin.

Another homologous oxygenase effector protein is P2 from the phenol hydroxylase system. Like MMOB, P2 is crucial to assuring efficient catalysis, and, although the detailed role of P2 is still emerging, this effector is known to increase significantly the yield of product during catalysis (*6*). Since both P2 and MMOB are found in functionally related systems and are positive catalytic activators operating via complex formation, it seems likely that their mechanisms of action will turn out to be quite similar when they are completely characterized. Accordingly, P2 and MMOB are sequentially and structurally more similar to each other than to putidaredoxin (see Figure 10). Using a best fit model, P2 is 25% sequentially identical and 55% similar to MMOB (see Figure 1). Nevertheless, there are significant differences in their overall folding. A comparison of NMR solution structures shows that both MMOB and P2 are comprised of two structural domains. P2 structural domain one ($\beta\alpha\beta$) (residues 1−47) has the α-helix folded onto an antiparallel β-sheet comprised of β-strands 1 and 2. In structural domain one of

[2] Zhang, X. Y., and Lipscomb, J. D., unpublished results.

MMOB ($\beta\alpha\beta\beta$) (residues 28−80 homologous to P2), the amino acid sequence following this first α-helix is longer than it is in P2 and allows formation of a third β-strand; these three strands align in an antiparallel β-sheet with the α-helix folded on top of strands 2 and 3.

Although secondary structural characteristics of domain two from MMOB ($\beta\alpha\alpha\beta\beta$) (residues 82−126) and P2 ($\beta\alpha\alpha\beta\beta\beta$) (residues 48−90) are essentially the same, domain two of P2 is considerably less compact than that of MMOB. A striking feature of domain two in P2 is the presence of a relatively large open cavity, a feature clearly absent in MMOB. It should be noted, however, that the P2 structure is relatively low resolution (backbone RMSD of 2.48 Å), and the appearance of this cavity may result from an insufficient number of long-range NOEs available for structural modeling. Moreover, NMR spectra for P2 show a number of unassignable resonances (*6*) which the authors ascribe to the presence of "a minor conformation of P2 coexisting with the major conformation". Given the tendency of MMOB to dimerize that we have demonstrated here, this conformational heterogeneity in P2 may, in fact, arise from similar self-association which would detract from elucidation of a higher resolution structure.

Another very significant structural difference between MMOB and P2, as well as the effector proteins of the other aromatic hydroxylases listed above, is that MMOB has a number of additional residues at the N-terminus. Compared to P2, MMOB has 33 additional N-terminal residues which account for much of its additional molecular weight. Studies have shown that MMOB devoid of these N-terminal residues is inactive, suggesting that these residues are important in some way for function[3] (*89*). Here, it was demonstrated that this N-terminal region is highly mobile and lacks stable secondary structure. However, analysis of circular dichroic data indicates that the amount of β-sheet derived from CD is the same as that from the NMR structure, whereas the amount of α-helix derived from CD is considerably greater. This difference in helix content suggests that the more flexible N-terminus (and possibly C-terminus) could form transient helix conformation, not differentiable as well-structured helix by NMR.

A further difference between MMOB and P2 is the lack of a substrate binding interaction with MMOB as interpreted by the absence of chemical shift changes in the protein when the MMOB solution was saturated with methane or furan. When phenol was added to P2, resonances arising from nuclei of W61 and D62, which were assigned to some minor conformation of the protein, disappeared (*6*). Since these residues are proximal to the cavity in the protein described above, the authors (*6*) postulated that this cavity may serve to bind phenol and to present it to the active site in the hydroxylase component as the two components form a complex during catalysis. The absence of such a "cavity" in MMOB may derive from the fact that methane is much smaller than phenol such that a discrete cavity may not be necessary or even discernible. On the other hand, the presence of those resonances in NMR spectra of P2, which were associated with the "unknown" minor conformation of P2, may be the result of self-association as noted here with homologous MMOB which self-associates in the millimolar concentration range. Therefore, phenol may in fact only be shifting the self-association equilibrium for P2 and not directly interacting with the protein.

Earlier studies demonstrated that MMOB forms a strong and specific complex with the α-subunit of MMOH (*35*). The structure of this complex and the effects that its formation may have on the conformation of MMOH and/or MMOB are unknown. Since the effects of complexation are readily observed in the optical and EPR spectroscopic characteristics of the MMOH metal center, it is reasonable that the MMOB−MMOH complex involves interaction of component surfaces near the binuclear iron cluster. Indeed, it has been pointed out that the intersection of the symmetrical MMOH $\alpha\beta\gamma$ protomers defines a deep groove or "canyon" in the structure over the binuclear iron site (*27*). In the region of the active site, this "canyon" has a substantial negatively charged surface potential, and it is known that the most important MMOH−MMOB interactions are electrostatic in nature[3] (*35*). The structure we report here shows that MMOB does have a few positively charged areas that might be important for MMOB to bind to MMOH. The most clustered positively charged area is near a turn in the protein between residues K58−K63. This small stretch of residues contains three lysines and extends out of the protein into the solution. NMR and modeling studies are now in progress using the X-ray crystal coordinates of MMOH to probe the potential interactions between the MMOB and MMOH.

In summary, MMOB has been the most extensively studied of any non-heme oxygenase effector protein due to the fact that it was the first of its class to be recognized and that it causes such dramatic effects in MMO catalysis. The availability of this structure of MMOB makes it possible for the first time to identify likely surface residues and/or protein folding domains that may mediate the interaction with MMOH. Although complex formation and conformational change are major engines of biological catalysis, little is known about the specific mode of action of oxygenase effector proteins. As structural data becomes available for the components of MMO, it becomes increasingly feasible to probe their mechanism of action at the molecular level. This information should be broadly applicable in studies of the effects of conformational change ranging from regulation of electron transfer, to control of substrate accessibility, to the promotion of the cleavage of the oxygen−oxygen bond.

SUPPORTING INFORMATION AVAILABLE

One table giving ^{1}H, ^{15}N, and ^{13}C chemical shifts for the protein MMOB is provided. This material is available free of charge via the Internet at http://pubs.acs.org.

REFERENCES

1. Tyson, C. A., Lipscomb, J. D., and Gunsalus, I. C. (1972) *J. Biol. Chem. 247*, 5777−5784.
2. Gunsalus, I. C., Meeks, J. R., Lipscomb, J. D., Marshall, V. P., Debrunner, P. G., and Münck, E. (1974) in *Molecular Mechanisms of Oxygen Activation* (Hayaishi, O., Ed.) pp 561−613, Academic Press, New York.
3. Newman, L. M., and Wackett, L. P. (1995) *Biochemistry 34*, 14066−14076.
4. Pikus, J. D., Studts, J. M., Achim, C., Kauffmann, K. E., Münck, E., Steffan, R. J., McClay, K., and Fox, B. G. (1996) *Biochemistry 35*, 9106−9119.

[3] Wallar, B. J., and Lipscomb, J. D., manuscript in preparation.

5. Whited, G. M., and Gibson, D. T. (1991) *J. Bacteriol. 173* 3010−3016.
6. Qian, H., Edlund, U., Powlowski, J., Shingler, V., and Sethson, I. (1997) *Biochemistry 36*, 495−504.
7. Small, F. J., and Ensign, S. A. (1997) *J. Biol. Chem. 272*, 24913−24920.
8. Miura, A., and Dalton, H. (1995) *Biosci. Biotech. Biochem. 59*, 853−859.
9. Green, J., and Dalton, H. (1985) *J. Biol. Chem. 260*, 15795−15801.
10. Fox, B. G., Froland, W. A., Dege, J. E., and Lipscomb, J. D. (1989) *J. Biol. Chem. 264*, 10023−10033.
11. Wallar, B. J., and Lipscomb, J. D. (1996) *Chem. Rev. 96*, 2625−2657.
12. Feig, A. L., and Lippard, S. J. (1994) *Chem. Rev. 94*, 759−805.
13. Lipscomb, J. D. (1994) *Ann. Rev. Microbiol. 48*, 371−399.
14. Dalton, H. (1980) *Adv. Appl. Microbiol. 26*, 71−87.
15. Takeguchi, M., Miyakawa, K., and Okura, I. (1998) *J. Mol. Catalysis A-Chemical 132*, 145−153.
16. Nguyen, H. H., Elliott, S. J., Yip, J. H., and Chan, S. I. (1998) *J. Biol. Chem. 273*, 7957−66.
17. Zahn, J. A., and DiSpirito, A. A. (1996) *J. Bacteriol. 178*, 1018−1029.
18. Semrau, J. D., Zolandz, D., Lidstrom, M. E., and Chan, S. I. (1995) *J. Inorg. Biochem. 58*, 235−244.
19. Stanley, S. H., Prior, S. D., Leak, D. J., and Dalton, H. (1983) *Biotech. Lett. 5*, 487−492.
20. Anthony, C. (1982) *The Biochemistry of Methylotrophs*, Academic Press, London.
21. Sato, R., and Omura, T. (1978) *Cytochrome P-450*, Academic Press, New York.
22. Omura, T., Ishimura, Y., and Fujii-Kuriyama, Y. (1993) *Cytochrome P-450*, Academic Press, New York.
23. Woodland, M. P., Patil, D. S., Cammack, R., and Dalton, H. (1986) *Biochim. Biophys. Acta 873*, 237−242.
24. Fox, B. G., Surerus, K. K., Münck, E., and Lipscomb, J. D. (1988) *J. Biol. Chem. 263*, 10553−10556.
25. Elango, N., Radhakrishnan, R., Froland, W. A., Wallar, B. J., Earhart, C. A., Lipscomb, J. D., and Ohlendorf, D. H. (1997) *Protein Sci. 6*, 556−568.
26. Rosenzweig, A. C., Nordlund, P., Takahara, P. M., Frederick, C. A., and Lippard, S. J. (1995) *Chem. Biol. 2*, 409−418.
27. Rosenzweig, A. C., Frederick, C. A., Lippard, S. J., and Nordlund, P. (1993) *Nature 366*, 537−543.
28. Fox, B. G., Hendrich, M. P., Surerus, K. K., Andersson, K. K., Froland, W. A., Lipscomb, J. D., and Münck, E. (1993) *J. Am. Chem. Soc. 115*, 3688−3701.
29. DeWitt, J. G., Bentsen, J. G., Rosenzweig, A. C., Hedman, B., Green, J., Pilkington, S., Papaefthymiou, G. C., Dalton, H., Hodgson, K. O., and Lippard, S. J. (1991) *J. Am. Chem. Soc. 113*, 9219−9233.
30. DeWitt, J. G., Rosenzweig, A. C., Salifoglou, A., Hedman, B., Lippard, S. J., and Hodgson, K. O. (1995) *Inorg. Chem. 34*, 2505−2515.
31. Lee, S.-K., Nesheim, J. C., and Lipscomb, J. D. (1993) *J. Biol. Chem. 268*, 21569−21577.
32. Lee, S.-K., Fox, B. G., Froland, W. A., Lipscomb, J. D., and Münck, E. (1993) *J. Am. Chem. Soc. 115*, 6450−6451.
33. Liu, Y., Nesheim, J. C., Lee, S.-K., and Lipscomb, J. D. (1995) *J. Biol. Chem. 270*, 24662−24665.
34. Liu, K. E., Wang, D., Huynh, B. H., Edmondson, D. E., Salifoglou, A., and Lippard, S. J. (1994) *J. Am. Chem. Soc. 116*, 7465−7466.
35. Fox, B. G., Liu, Y., Dege, J. E., and Lipscomb, J. D. (1991) *J. Biol. Chem. 266*, 540−550.
36. Pulver, S. C., Froland, W. A., Lipscomb, J. D., and Solomon, E. I. (1997) *J. Am. Chem. Soc. 119*, 387−395.
37. Liu, Y., Nesheim, J. C., Paulsen, K. E., Stankovich, M. T., and Lipscomb, J. D. (1997) *Biochemistry 36*, 5223−5233.
38. Paulsen, K. E., Liu, Y., Fox, B. G., Lipscomb, J. D., Münck, E., and Stankovich, M. T. (1994) *Biochemistry 33*, 713−722.
39. Froland, W. A., Andersson, K. K., Lee, S.-K., Liu, Y., and Lipscomb, J. D. (1992) *J. Biol. Chem. 267*, 17588−17597.
40. Pochapsky, T. C., Ye, X. M., Rathnaswamy, G., and Lyon, T. A. (1994) *Biochemistry 33*, 6424−6432.
41. Powlowski, J., and Shingler, V. (1994) *Biodegradation 5*, 219−236.
42. Nordlund, I., Powlowski, J., and Shingler, V. (1990) *J. Bacteriol. 172*, 6826−6833.
43. Thompson, J. D., Higgins, D. G., and Gibson, T. J. (1994) *Nucleic Acids Res. 22*, 4673−4680.
44. Cardy, D. L., Laidler, V., Salmond, G. P., and Murrell, J. C. (1991) *Mol. Microbiol. 5*, 335−342.
45. Koga, H., Yamaguchi, E., Matsunaga, K., Aramaki, H., and Horiuchi, T. (1989) *J. Biochem. (Tokyo) 106*, 831−836.
46. Cardy, D. L., Laidler, V., Salmond, G. P., and Murrell, J. C. (1991) *Arch. Microbiol. 156*, 477−483.
47. Tsien, H. C., and Hanson, R. S. (1992) *Appl. Environ. Microbiol. 58*, 953−960.
48. Tabor, S., and Richardson, C. C. (1985) *Proc. Natl. Acad. Sci. U.S.A. 82*, 1074−1078.
49. Sambrook, J., Fritsch, E. F., and Maniatis, T. (1989) *Molecular cloning: A laboratory manual*, Cold Spring Harbor Laboratory, Cold Spring Harbor, NY.
50. Delaglio, F., Grzesiek, S., Vuister, G. W., Zhu, G., Pfeifer, J., and Bax, A. (1995) *J. Biol. NMR 6*, 277−293.
51. Garrett, D. S., Powers, R., Gronenborn, A. M., and Clore, G. M. (1991) *J. Magn. Reson. 94*, 214−220.
52. Karger, J., Pfeifer, H., and Heink, W. (1988) *Adv. Magn. Reson. 12*, 1−89.
53. Tillett, M. L., Lian, L. Y., and Norwood, T. J. (1998) *J. Magn. Res. 133*, 379−384.
54. Mayo, K. H., Ilyina, E., and Park, H. (1996) *Protein Sci. 5*, 1301−1315.
55. Cantor, C. R., and Schimmel, P. R. (1980) in *Biophysical Chemistry, Part III: The behavior of biological macromolecules*, pp 979−1039, W. H. Freeman, New York, NY.
56. Zhang, O., Kay, L. E., Olivier, J. P., and Forman-Kay, J. D. (1994) *J. Biomol. NMR 4*, 845−858.
57. Muhandiram, D. R., Farrow, N. A., Xu, G. Y., Smallcombe, S. H., and Kay, L. E. (1993) *J. Magn. Res. B 102*, 317−321.
58. Grzesiek, S., Anglister, J., and Bax, A. (1993) *J. Magn. Res. B 101*, 114−119.
59. Lyons, B. A., and Montelione, G. T. (1993) *J. Magn. Res. B 101*, 206−209.
60. Yamazaki, T., Lee, W., Revington, M., Mattiello, D. L., Dahlquist, F. W., Arrowsmith, C. H., and Kay, L. E. (1994) *J. Am. Chem. Soc. 116*, 6464.
61. Muhandiram, D. R., and Kay, L. E. (1994) *J. Magn. Res. B 103*, 203−216.
62. Kay, L. E., Xu, G. Y., Singer, A. U., Muhandiram, D. R., and Forman-Kay, J. D. (1993) *J. Magn. Res. B 101*, 333−337.
63. Kuboniwa, H., Grzesiek, S., Delaglio, F., and Bax, A. (1994) *J. Biomol. NMR 4*, 871−878.
64. Vuister, G. W., and Bax, A. (1993) *J. Am. Chem. Soc. 115*, 7772−7777.
65. Kay, L. E., Keifer, P., and Saarinen, T. (1992) *J. Am. Chem. Soc. 114*, 10663−10665.
66. Wider, G., Macura, S., Anil-Kumar, Ernst, R. R., and Wüthrich, K. (1984) *J. Magn. Reson. 56*, 207−234.
67. Yamazaki, T., Forman-Kay, J. D., and Kay, L. E. (1993) *J. Am. Chem. Soc. 115*, 11054.
68. Farmer, B., Lavoie, T., Mueller, L., and Metzler, W. (1995) *J. Magn. Reson. B 107*, 197−200.
69. Garrett, D. S., Seok, Y. J., Liao, D. I., Peterkofsky, A., Gronenborn, A. M., and Clore, G. M. (1997) *Biochemistry 36*, 2517−2530.
70. Wüthrich, K., Billeter, M., and Braun, W. (1983) *J. Mol. Biol. 169*, 949−961.
71. Koning, T. M. G., Boelens, R., and Kaptein, R. (1990) *J. Magn. Res. 90*, 111−123.
72. Tropp, J. (1980) *J. Chem. Phys. 72*, 6035−6043.
73. Brunger, A. T., Clore, G. M., Gronenborn, A. M., and Karplus, M. (1986) *Proc. Natl. Acad. Sci. U.S.A. 83*, 3801−3805.
74. Clore, G. M., Brunger, A. T., Karplus, M., and Gronenborn, A. M. (1986) *J. Mol. Biol. 191*, 523−551.

75. Senior, M. M., Frederick, A. F., Black, S., Murgolo, N. J., Perkins, L. M., Wilson, O., Snow, M. E., and Wang, Y. S. (1998) *J. Biomol. NMR 11*, 153−164.
76. Bruenger, A. T. (1993) *X-PLOR Version 3.1 Manual*, Yale University, New Haven, CT.
77. Nilges, M., Kuszewski, J., and Bruenger, A. T. (1991) in *Computational aspects of the study of biological macromolecules by nuclear magnetic resonance spectroscopy* (Hoch, J., Ed.), Plenum Press, New York.
78. Powell, M. J. D. (1977) *Math. Program. 12*, 241−254.
79. Nilges, M., Clore, G. M., and Gronenborn, A. M. (1988) *FEBS Lett. 229*, 317−324.
80. Koradi, R., Billeter, M., and Wüthrich, K. (1996) *J. Mol. Graphics 14*, 51−55.
81. Teller, D. C., Swanson, E., and de Haen, C. (1979) *Meth. Enzymol. 61*, 103−124.
82. Mills, R. (1973) *J. Phys. Chem. 77*, 685−688.
83. Laskowski, R. A., MacArthur, M. W., Moss, D. S., and Thornton, J. M. (1993) *J. Appl. Crystallogr. 26*, 283−291.
84. Johnson, W. C., Jr. (1990) *Proteins 7*, 205−214.
85. Provencher, S. W. (1982) *Comp. Phys. Commun. 27*, 229−242.
86. Fox, B. G., Shanklin, J., Somerville, C., and Münck, E. (1993) *Proc. Natl. Acad. Sci. U.S.A. 90*, 2486−2490.
87. Lipscomb, J. D., Sligar, S. G., Namtvedt, M. J., and Gunsalus, I. C. (1976) *J. Biol. Chem. 251*, 1116−1124.
88. Rypniewski, W. R., Breiter, D. R., Benning, M. W., Wesenberg, G., Oh, B.-H., Markley, J. L., Rayment, I., and Holden, H. M. (1991) *Biochemistry 30*, 4126−4131.
89. Lloyd, J. S., Bhambra, A., Murrell, J. C., and Dalton, H. (1997) *Eur. J. Biochem. 248*, 72−79.

BI982992F